

# Hybrid Heterocycle-Containing Electron-Transport Materials Synthesized by Regioselective Suzuki Cross-Coupling Reactions for Highly Efficient Phosphorescent OLEDs with Unprecedented Low Operating Voltage

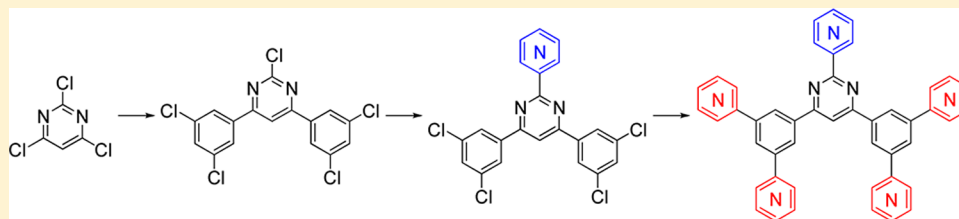
Ming Liu,<sup>†</sup> Shi-Jian Su,<sup>\*,†</sup> Min-Cherl Jung,<sup>‡</sup> Yabing Qi,<sup>\*,‡</sup> Wei-Ming Zhao,<sup>§</sup> and Junji Kido<sup>||</sup>

<sup>†</sup>State Key Laboratory of Luminescent Materials and Devices and Institute of Polymer Optoelectronic Materials and Devices, South China University of Technology, Guangzhou 510640, China

<sup>‡</sup>Energy Materials and Surface Sciences Unit, Okinawa Institute of Science and Technology Graduate University, 1919-1 Tancha, Onna-son, Kunigami-gun, Okinawa 904-0495, Japan

<sup>§</sup>Dongguan LITEWELL Technology Incorporation, Dongguan 523656, China

<sup>||</sup>Department of Organic Device Engineering, Graduate School of Science and Engineering, Yamagata University, 4-3-16 Jonan, Yonezawa, Yamagata 992-8510, Japan



**ABSTRACT:** A series of hybrid heterocycle-containing electron-transport materials (ETMs) with different pyridine substitution positions in a single molecule were successfully synthesized by regioselective sequential palladium-catalyzed Suzuki cross-coupling reactions. B3LYP calculations show that the experimental regioselectivity is consistent with the trends in calculated bond dissociation energies of the carbon–halogen (C–X) bonds of the reactants and intermediates. The two carbon species associated with C–N and C–C can be detected by X-ray photoelectron spectroscopy. Extremely low turn-on voltages ( $V_{on}$ ) of 2.1 V for electroluminescence, which are readily 0.2–0.3 V lower than the minimum value of the emitted photon energy ( $h\nu$ )/ $e$ , were experimentally achieved by utilizing the developed ETMs as an electron-transport and hole/exciton-block layer for the classical *fac*-tris(2-phenylpyridine) iridium ( $\text{Ir}(\text{PPy})_3$ )-based green phosphorescent organic light-emitting devices (OLEDs). In addition, hitherto the lowest operating voltages of 2.39, 2.72, and 3.88 V for 100, 1000, and 10 000  $\text{cd m}^{-2}$  were achieved with simultaneously improved external quantum efficiency ( $\eta_{ext}$ ) to give a high power efficiency, and the operating voltage for 100  $\text{cd m}^{-2}$  is already corresponding to the value of  $h\nu/e$ . Atomic force microscopy measurements reveal morphological fine structure of the thin film samples of ETMs with a pyrimidine core, which possibly contributes to the low driving voltages that were achieved for the devices that are based on these ETMs. These findings indicate that aside from the ultralow operating voltage well-balanced carriers can be also achieved with a finely synthesized hybrid heterocycle-containing ETM as a nondoped electron-transport layer, and the B3LYP calculation is an effective method to predict the regioselective cross-coupling reactions for fine design of such an ETM.

**KEYWORDS:** regioselective, Suzuki cross-coupling reaction, phosphorescent OLEDs, electron-transport material, low operating voltage

## INTRODUCTION

Organic light-emitting devices (OLEDs) have become of considerable commercialization interest in recent years for their applications as eco-friendly solid-state lighting and next-generation full-color flat-panel displays. In the last two decades, many studies have focused on improving external quantum efficiency ( $\eta_{ext}$ ) of OLEDs,<sup>1</sup> and phosphorescent OLEDs have attracted tremendous attention since nearly 100% internal quantum efficiency of electroluminescence is readily achieved by harvesting both electro-generated singlet and triplet excitons.<sup>2</sup> It is well-known that at a given  $\eta_{ext}$  lower operating

voltage generally gives higher power conversion efficiency. As such, lowering operating voltage is also crucially important to reduce their electrical power consumption.<sup>3</sup> It has been reported that OLEDs with *p*-doped hole-transport layer (HTL) and *n*-doped electron-transport layer (ETL), called *p-i-n* OLEDs, generally exhibit low driving voltage as well as high power efficiency.<sup>4</sup> However, carrier and exciton block layers are absolutely essential to prevent exciton quenching in the

Received: March 25, 2012

Published: September 27, 2012

emissive layer (EML) by the *p* and *n* dopants, and the internal energy barriers to overcome the carrier and exciton block layers may induce voltage drop and thus higher operating voltage. More importantly, the approach of using *n* dopant-like alkaline metals might be hampered by stability issues and leads to manufacturing difficulties. It is thus of interest to utilize a single carrier transport layer instead of *p*- or *n*-doped layer and carrier/exciton block layer. In the past years, a series of multifunctional pyridine-containing electron-transport materials (ETMs) have been developed as an ETL as well as a hole/exciton block layer for the phosphorescent OLEDs, leading to a simplified device structure and an improved  $\eta_{\text{ext}}$ .<sup>7</sup> Most recently, operating voltages that are readily lower than those of the *p-i-n* OLEDs were also achieved by utilizing 1,3,5-triazine-containing ETMs.<sup>7d</sup> A general character for all these ETMs is that they have pyridine rings on the periphery of the molecule and the substituted positions of the pyridine rings in a single molecule are identical. Since the nitrogen atom position of the substituted pyridine ring was found to be a key factor in determining the electron injection and transport property and thus the OLED performance,<sup>8</sup> it is of interest to synthesize pyridine-containing compounds with different pyridine substitution positions in a single molecule to further tune the property of the pyridine-containing ETMs. Besides this, simultaneous introduction of other heterocycles to give hybrid heterocycle-containing compounds is also an attractive approach to tune their property.

A general synthetic method for the pyridine-containing ETMs is the Suzuki cross-coupling reaction. To obtain pyridine-containing compounds with different substituted positions in a single molecule, selective sequential cross-coupling reactions involving multihalogenated aromatics should be an effective approach. For the Suzuki cross-coupling reactions, the nature of the halogen that is being displaced has been reported as one source of selectivity. In this article, we report on pyridine-containing ETMs with different pyridine substitution positions in a single molecule that are successfully synthesized by regioselective palladium-catalyzed Suzuki cross-coupling reactions of organoboron compounds and aryl halides, although the halogens being displaced are identical for the reactants and the intermediates. In addition, pyrimidine ring was simultaneously introduced to give hybrid heterocycle-containing ETMs. Bond dissociation energies (BDEs) of the aryl halides were calculated with B3LYP, and the trends in the calculated BDEs are consistent with the experimental regioselectivity. As proven by the experimental and calculation results, their energy levels can be finely tuned by the different pyridine substitution positions as well as the introduction of pyrimidine. In addition, their structure–property relationships were thoroughly studied by thermal analysis (TA), X-ray photoelectron spectroscopy (XPS) analysis, atomic force microscopy (AFM), and device application. Simultaneous improvement of  $\eta_{\text{ext}}$  and unprecedented low operating voltage were achieved for the classical *fac*-tris(2-phenylpyridine) iridium (Ir(PPy)<sub>3</sub>) based green phosphorescent OLEDs by utilizing the developed hybrid heterocycle-containing ETMs.

## EXPERIMENTAL SECTION

**General.** <sup>1</sup>H and <sup>13</sup>C NMR spectra were recorded on Varian 500 (500 MHz) spectrometer. Mass spectra were obtained using a JEOL JMS-K9 mass spectrometer. Differential scanning calorimetry (DSC) was performed using a Perkin-Elmer Diamond DSC Pyris instrument under nitrogen atmosphere at a heating rate of 10 °C min<sup>-1</sup>.

Thermogravimetric analysis (TGA) was undertaken using a SEIKO EXSTAR 6000 TG/DTA 6200 unit under nitrogen atmosphere at a heating rate of 10 °C min<sup>-1</sup>. UV–vis absorption spectra were measured using a Shimadzu UV-3150 UV–vis-NIR spectrophotometer. Steady-state photoluminescent spectra were obtained at room temperature using a FluoroMax-2 (Jobin–Yvon–Spex) luminescence spectrometer. Ionization potentials were determined by atmospheric ultraviolet photoelectron spectroscopy (Rikken Keiki AC-3). The ETMs were transported in sealed containers that were backfilled with dry nitrogen gas to Okinawa Institute of Science and Technology Graduate University for further analysis. The ETMs were kept in a dry N<sub>2</sub> storage box prior to use to minimize exposure to air. A two-chamber ultrahigh vacuum (UHV) system (Omicron NanoTechnology GmbH) was used to perform *in situ* X-ray photoelectron spectroscopy (XPS). The ETMs were introduced to the preparation chamber of the UHV system in quartz crucibles held by tungsten wires for resistive heating. A quartz crystal microbalance was used to monitor evaporation rate and film thickness. After thorough outgassing, thin film samples (thickness ~30 nm) were prepared by evaporating ETMs on precleaned indium–tin oxide (ITO) glass substrates (Geomatec Co. Ltd., 5 Ω/sq) at evaporation rates of ~0.2 Å/s.

An unmonochromated Mg Kα (1253.6 eV) X-ray source and EA125 energy analyzer with single channeltron were used for XPS measurements. The pass energy of electron analyzer and the energy resolution of XPS measurements are 20 and 0.9 eV, respectively. The chemical states of all samples were obtained for the C 1s and N 1s regions. The binding energies were calibrated with respect to the Au 4f<sub>7/2</sub> level (at a binding energy of 84.0 eV).<sup>9</sup> Following the XPS measurements, the samples were taken out of the UHV system to investigate their surface morphology properties. Topography images of the samples were acquired in air by atomic force microscopy (ASYLUM Research MFP 3D) in the tapping mode using Al coated silicon cantilevers with spring constants of 48 N/m at resonant frequency of 190 kHz.

**Synthesis.** All the reagents were purchased from Sigma-Aldrich and were used without further purification. 3-(3-(4,4,5,5-Tetramethyl-1,3,2-dioxaborolan-2-yl)phenyl)pyridine (**15**) was synthesized according to the literature procedures.<sup>7b</sup> **1–6** were synthesized according to regioselective palladium-catalyzed Suzuki cross-coupling reactions of organoboron compounds and aryl halides.

**1,3-Dibromo-5-pyrid-3-yl-benzene (9).** A mixture of 1,3,5-tribromobenzene (**7**) (18.9 g, 60 mmol), 3-(4,4,5,5-tetramethyl-1,3,2-dioxaborolan-2-yl)pyridine (**8**) (12.3 g, 60 mmol), tetrakis(triphenylphosphine) palladium(0) (Pd(PPh<sub>3</sub>)<sub>4</sub>) (0.693 g, 0.6 mmol), and 2 M Na<sub>2</sub>CO<sub>3</sub> (70 mL) in toluene (200 mL) and ethanol (67 mL) was stirred at 85 °C for 12 h under nitrogen atmosphere. After cooling to room temperature, the mixture was poured into water and then extracted with toluene. The combined organic phase was washed with brine and dried over MgSO<sub>4</sub>. The subjection of the crude mixture to silica gel chromatography (eluent: chloroform/ethyl acetate = 1/1) afforded **9** (9.33 g, 50%) as white powder, accompanied by a 16% yield of 1-bromo-3,5-dipyrid-3-yl-benzene (**18**) (2.93 g). <sup>1</sup>H NMR (270 MHz, CDCl<sub>3</sub>, δ): 8.80 (d, *J* = 2.4 Hz, 1H), 8.66 (dd, *J* = 1.6 and 5.0 Hz, 1H), 7.85–7.81 (m, 1H), 7.72 (t, *J* = 1.6 Hz, 1H), 7.66 (d, *J* = 1.6 Hz, 2H), 7.42–7.37 (m, 1H). **18** <sup>1</sup>H NMR (270 MHz, CDCl<sub>3</sub>, δ): 8.88 (d, *J* = 2.4 Hz, 2H), 8.67 (dd, *J* = 1.0 and 4.8 Hz, 2H), 7.93–7.89 (m, 2H), 7.77 (t, *J* = 1.0 Hz, 2H), 7.69 (s, 1H), 7.45–7.40 (m, 2H).

**1,3-Bis(3,5-dichlorophenyl)-5-pyrid-3-yl-benzene (11).** A mixture of **9** (1.79 g, 5.72 mmol), 3,5-dichlorophenyl boronic acid (**10**) (2.62 g, 13.7 mmol), Pd(PPh<sub>3</sub>)<sub>4</sub> (0.661 g, 0.572 mmol), and 2 M K<sub>2</sub>CO<sub>3</sub> (50 mL) in toluene (100 mL) and ethanol (40 mL) was stirred at 85 °C for 22 h under nitrogen atmosphere. After cooling to room temperature, the mixture was poured into water and then extracted with chloroform. The combined organic phase was washed with brine and dried over MgSO<sub>4</sub>. The subjection of the crude mixture to silica gel chromatography (eluent: chloroform) afforded **11** (1.69 g, 66%) as white powder. <sup>1</sup>H NMR (400 MHz, CDCl<sub>3</sub>, δ): 8.933 (d, *J* = 2.3 Hz,

1H), 8.682 (d,  $J = 5.0$  Hz, 1H), 7.981–7.962 (m, 1H), 7.740 (d,  $J = 1.8$  Hz, 2H), 7.701 (s, 1H), 7.552 (s, 4H), 7.458–7.422 (m, 3H).

**1,3-Bis(3,5-dipyrid-3-ylphenyl)-5-pyrid-3-yl-benzene (1).** A mixture of **11** (1.69 g, 3.80 mmol), **8** (4.05 g, 19.8 mmol), tris(dibenzylideneacetone) dipalladium(0) ( $\text{Pd}_2(\text{dba})_3$ ) (139 mg, 0.152 mmol), tricyclohexylphosphine ( $\text{PCy}_3$ ) (102 mg, 0.365 mmol), and  $\text{K}_3\text{PO}_4$  (15.5 g, 73 mmol) in 1,4-dioxane (300 mL) and water (70 mL) was stirred at 90 °C for 24 h under nitrogen atmosphere. After cooling to room temperature, the mixture was poured into water and then extracted with chloroform. The combined organic phase was washed with brine and dried over  $\text{MgSO}_4$ . The subjection of the crude mixture to silica gel chromatography (eluent: chloroform/methanol = 15/1) afforded **1** (1.92 g, 82%) as white powder.  $^1\text{H}$  NMR (500 MHz,  $\text{CDCl}_3$ ,  $\delta$ ): 9.008–9.001 (m, 1H), 8.980–8.973 (m, 4H), 8.683–8.659 (m, 5H), 8.054–7.984 (m, 6H), 7.924–7.919 (m, 6H), 7.820–7.811 (m, 2H), 7.466–7.427 (m, 5H).  $^{13}\text{C}$  NMR (500 MHz,  $\text{CDCl}_3$ ,  $\delta$ ): 149.118, 148.465, 148.435, 142.549, 142.373, 139.764, 139.699, 136.201, 136.117, 134.736, 134.702, 126.199, 126.085, 125.944, 125.677, 123.769. EIMS ( $m/z$ ):  $[\text{M}^+]$  calcd, 815.72; found, 816. Anal. Calc. for  $\text{C}_{43}\text{H}_{29}\text{N}_5$  (%): C, 83.88; H, 4.75; N, 11.37. Found: C, 83.65; H, 4.82; N, 11.48.

**1,3-Bis(3,5-dipyrid-4-ylphenyl)-5-pyrid-3-yl-benzene (2).** **2** was synthesized in a similar manner to that of **1**. Yield: 41%.  $^1\text{H}$  NMR (500 MHz,  $\text{CDCl}_3$ ,  $\delta$ ): 9.012 (d,  $J = 2.5$  Hz, 1H), 8.767–8.755 (m, 8H), 8.690 (dd,  $J = 1.5$  and 5.0 Hz, 1H), 8.047–8.025 (m, 1H), 8.001–7.998 (m, 4H), 7.954 (t,  $J = 1.5$  Hz, 1H), 7.931–7.928 (m, 4H), 7.652–7.640 (m, 8H), 7.469–7.444 (m, 1H).  $^{13}\text{C}$  NMR (500 MHz,  $\text{CDCl}_3$ ,  $\delta$ ): 150.586, 149.285, 148.542, 147.565, 142.667, 142.255, 140.287, 139.871, 136.037, 134.641, 126.749, 126.165, 126.081, 125.391, 123.746, 121.854. EIMS ( $m/z$ ):  $[\text{M}^+]$  calcd, 815.72; found, 816. Anal. Calc. for  $\text{C}_{43}\text{H}_{29}\text{N}_5$  (%): C, 83.88; H, 4.75; N, 11.37. Found: C, 83.60; H, 4.68; N, 11.57.

**2-Chloro-4,6-bis(3,5-dichlorophenyl)pyrimidine (14).** A mixture of 2,4,6-trichloropyrimidine (**13**) (5.50 g, 30 mmol), **10** (12.0 g, 63 mmol), bis(triphenylphosphine)palladium(II) chloride ( $\text{PdCl}_2(\text{PPh}_3)_2$ ) (842 mg, 1.2 mmol), and 2 M  $\text{K}_2\text{CO}_3$  (60 mL) in acetonitrile (150 mL) was stirred at 50 °C for 20 h under nitrogen atmosphere. After cooling to room temperature, the mixture was poured into water and then extracted with chloroform. The combined organic phase was washed with brine and dried over  $\text{MgSO}_4$ . The subjection of the crude mixture to silica gel chromatography (eluent: chloroform/*n*-hexane = 2/1) afforded **14** (11.2 g, 92%) as white powder.  $^1\text{H}$  NMR (500 MHz,  $\text{CDCl}_3$ ,  $\delta$ ): 8.041 (d,  $J = 2.0$  Hz, 4H), 7.909 (s, 1H), 7.565 (t,  $J = 1.8$  Hz, 2H). EIMS ( $m/z$ ):  $[\text{M}^+]$  calcd, 404.51; found, 404.

**2-Pyrid-3-yl-4,6-bis(3,5-dichlorophenyl)pyrimidine (16).** A mixture of **14** (4.05 g, 10 mmol), **8** (2.26 g, 11 mmol),  $\text{PdCl}_2(\text{PPh}_3)_2$  (140 mg, 0.2 mmol), and 2 M  $\text{K}_2\text{CO}_3$  (50 mL) in 1,4-dioxane (120 mL) was stirred at 100 °C for 18 h under nitrogen atmosphere. After cooling to room temperature, the mixture was poured into water and then extracted with chloroform. The combined organic phase was washed with brine and dried over  $\text{MgSO}_4$ . The subjection of the crude mixture to silica gel chromatography (eluent: chloroform) afforded **16** (2.84 g, 64%) as white powder.  $^1\text{H}$  NMR (500 MHz,  $\text{CDCl}_3$ ,  $\delta$ ): 9.872 (d,  $J = 1.5$  Hz, 1H), 8.915–8.891 (m, 1H), 8.796 (dd,  $J = 1.5$  and 4.5 Hz, 1H), 8.156 (d,  $J = 2.0$  Hz, 4H), 7.938 (s, 1H), 7.572 (t,  $J = 1.8$  Hz, 2H), 7.521–7.495 (m, 1H). EIMS ( $m/z$ ):  $[\text{M}^+]$  calcd, 447.14; found, 448.

**4,6-Bis(3,5-dichlorophenyl)-2-(3-(pyridin-3-yl)phenyl)pyrimidine (17).** **17** was synthesized in a manner similar to that of **16**. Yield: 67%.  $^1\text{H}$  NMR (500 MHz,  $\text{CDCl}_3$ ,  $\delta$ ): 8.993 (d,  $J = 2.0$  Hz, 1H), 8.828 (t,  $J = 1.8$  Hz, 1H), 8.697 (dd,  $J = 1.5$  and 7.5 Hz, 1H), 8.672–8.659 (m, 1H), 8.130–8.113 (m, 4H), 8.032–8.008 (m, 1H), 7.878 (s, 1H), 7.769 (dd,  $J = 1.5$  and 7.5 Hz, 1H), 7.684 (t,  $J = 7.5$  Hz, 1H), 7.554–7.543 (m, 1H), 7.462–7.437 (m, 1H).  $^{13}\text{C}$  NMR (500 MHz,  $\text{CDCl}_3$ ,  $\delta$ ): 164.709, 162.897, 148.798, 148.504, 139.822, 138.395, 138.010, 136.427, 135.927, 134.577, 130.961, 130.060, 129.481, 128.363, 127.127, 125.780, 123.686, 110.716. EIMS ( $m/z$ ):  $[\text{M}^+]$  calcd, 523.24; found, 524.

**4,6-Bis(3,5-di(pyridin-3-yl)phenyl)-2-(pyridin-3-yl)pyrimidine (3).** **3** was synthesized in a manner similar to that of **1**. Yield: 87%.  $^1\text{H}$  NMR (500 MHz,  $\text{CDCl}_3$ ,  $\delta$ ): 9.959 (d,  $J = 2.0$  Hz, 1H), 9.030 (d,  $J = 2.0$  Hz, 4H), 8.991–8.967 (m, 1H), 8.799 (dd,  $J = 2.0$  and 5.0 Hz, 1H), 8.717 (dd,  $J = 2.0$  and 5.0 Hz, 4H), 8.523 (d,  $J = 1.5$  Hz, 4H), 8.246 (s, 1H), 8.079–8.055 (m, 4H), 7.968 (t,  $J = 1.8$  Hz, 2H), 7.536–7.509 (m, 1H), 7.505–7.478 (m, 4H).  $^{13}\text{C}$  NMR (500 MHz,  $\text{CDCl}_3$ ,  $\delta$ ): 164.671, 163.366, 151.785, 150.316, 149.382, 148.504, 139.967, 138.830, 135.847, 134.722, 133.078, 128.779, 125.857, 123.842, 123.522, 111.357. EIMS ( $m/z$ ):  $[\text{M}^+]$  calcd, 617.70; found, 618. Anal. Calc. for  $\text{C}_{41}\text{H}_{27}\text{N}_7$  (%): C, 79.72; H, 4.41; N, 15.87. Found: C, 79.54; H, 4.52; N, 15.65.

**4,6-Bis(3,5-di(pyridin-4-yl)phenyl)-2-(pyridin-3-yl)pyrimidine (4).** **4** was synthesized in a similar manner to that of **1**. Yield: 82%.  $^1\text{H}$  NMR (500 MHz,  $\text{CDCl}_3$ ,  $\delta$ ): 9.980 (d,  $J = 2.5$  Hz, 1H), 8.989–8.965 (m, 1H), 8.823–8.793 (m, 9H), 8.582 (d,  $J = 2.0$  Hz, 4H), 8.226 (s, 1H), 8.057 (t,  $J = 1.8$  Hz, 2H), 7.684 (dd,  $J = 2.0$  and 4.5 Hz, 8H), 7.552–7.527 (m, 1H).  $^{13}\text{C}$  NMR (500 MHz,  $\text{CDCl}_3$ ,  $\delta$ ): 164.625, 163.488, 151.907, 150.698, 150.373, 147.303, 140.490, 138.994, 135.805, 132.959, 128.512, 126.532, 123.553, 121.893, 111.445. EIMS ( $m/z$ ):  $[\text{M}^+]$  calcd, 617.70; found, 618. Anal. Calc. for  $\text{C}_{41}\text{H}_{27}\text{N}_7$  (%): C, 79.72; H, 4.41; N, 15.87. Found: C, 79.58; H, 4.55; N, 15.60.

**4,6-Bis(3,5-di(pyridin-3-yl)phenyl)-2-(3-(pyridin-3-yl)phenyl)pyrimidine (5).** **5** was synthesized in a similar manner to that of **1**. Yield: 60%.  $^1\text{H}$  NMR (500 MHz,  $\text{CDCl}_3$ ,  $\delta$ ): 9.035–9.030 (m, 4H), 8.995–8.990 (m, 1H), 8.949 (t,  $J = 1.8$  Hz, 1H), 8.801–8.780 (m, 1H), 8.710 (dd,  $J = 1.5$  and 4.5 Hz, 4H), 8.644 (dd,  $J = 2.0$  and 5.0 Hz, 1H), 8.513 (d,  $J = 1.5$  Hz, 4H), 8.205 (s, 1H), 8.075–8.051 (m, 4H), 8.036–8.013 (m, 1H), 7.959 (t,  $J = 1.8$  Hz, 2H), 7.799–7.778 (m, 1H), 7.713 (t,  $J = 7.5$  Hz, 1H), 7.499–7.472 (m, 4H), 7.444–7.417 (m, 1H).  $^{13}\text{C}$  NMR (500 MHz,  $\text{CDCl}_3$ ,  $\delta$ ): 164.947, 149.566, 148.983, 148.738, 148.670, 140.125, 139.461, 138.759, 138.534, 136.753, 136.143, 134.949, 134.762, 130.054, 129.761, 128.845, 128.590, 127.495, 126.148, 124.069, 123.920, 111.618. EIMS ( $m/z$ ):  $[\text{M}^+]$  calcd, 693.80; found, 694. Anal. Calc. for  $\text{C}_{47}\text{H}_{31}\text{N}_7$  (%): C, 81.36; H, 4.50; N, 14.13. Found: C, 81.22; H, 4.57; N, 13.95.

**4,6-Bis(3,5-di(pyridin-4-yl)phenyl)-2-(3-(pyridin-3-yl)phenyl)pyrimidine (6).** **6** was synthesized in a manner similar to that of **1**. Yield: 74%.  $^1\text{H}$  NMR (500 MHz,  $\text{CDCl}_3$ ,  $\delta$ ): 9.011–9.007 (m, 1H), 8.964 (s, 1H), 8.791 (dd,  $J = 1.5$  and 4.5 Hz, 8H), 8.660 (dd,  $J = 1.5$  and 5.0 Hz, 1H), 8.572 (d,  $J = 2.0$  Hz, 4H), 8.183 (s, 1H), 8.054–8.021 (m, 3H), 7.810 (d,  $J = 7.5$  Hz, 1H), 7.730 (t,  $J = 7.5$  Hz, 1H), 7.683 (dd,  $J = 1.5$  and 4.5 Hz, 8H), 7.445–7.420 (m, 1H). EIMS ( $m/z$ ):  $[\text{M}^+]$  calcd, 693.80; found, 694. Anal. Calc. for  $\text{C}_{47}\text{H}_{31}\text{N}_7$  (%): C, 81.36; H, 4.50; N, 14.13. Found: C, 81.19; H, 4.59; N, 14.02.

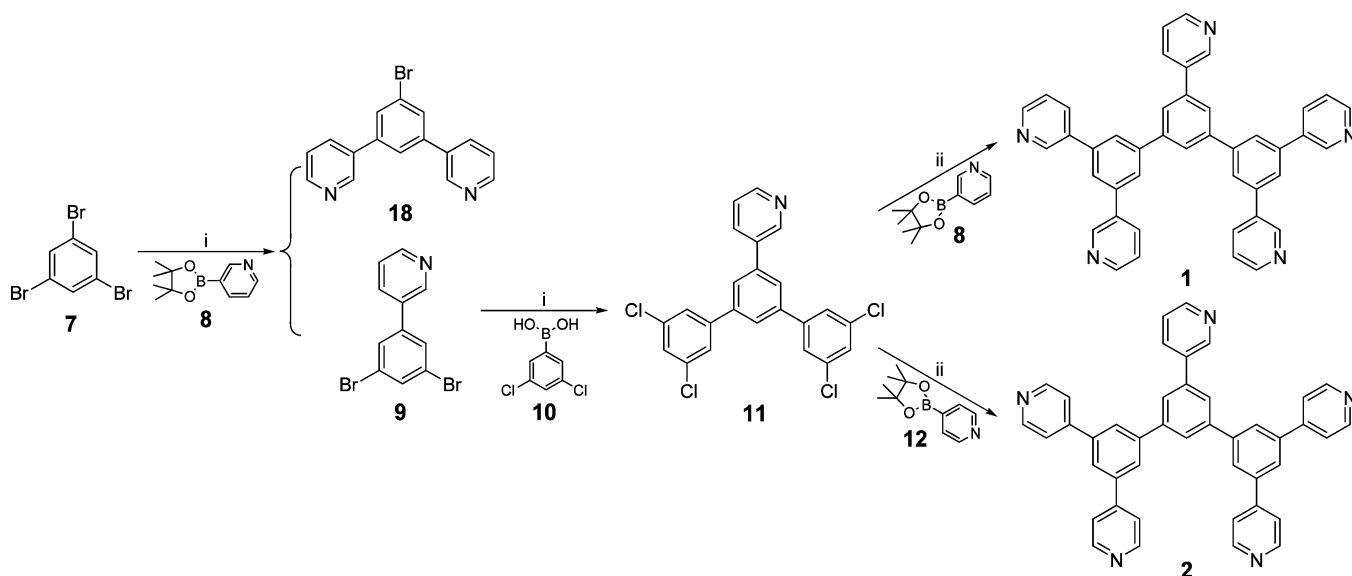
**Computations.** BDEs of carbon–halogen (C–X) bonds of aryl halides were calculated using the Gaussian suite of programs (Gaussian 03W) with UB3LYP/6-31G(d) method. BDE is defined as the change in enthalpy,  $\Delta H$ , for homolysis of the C–X bond.



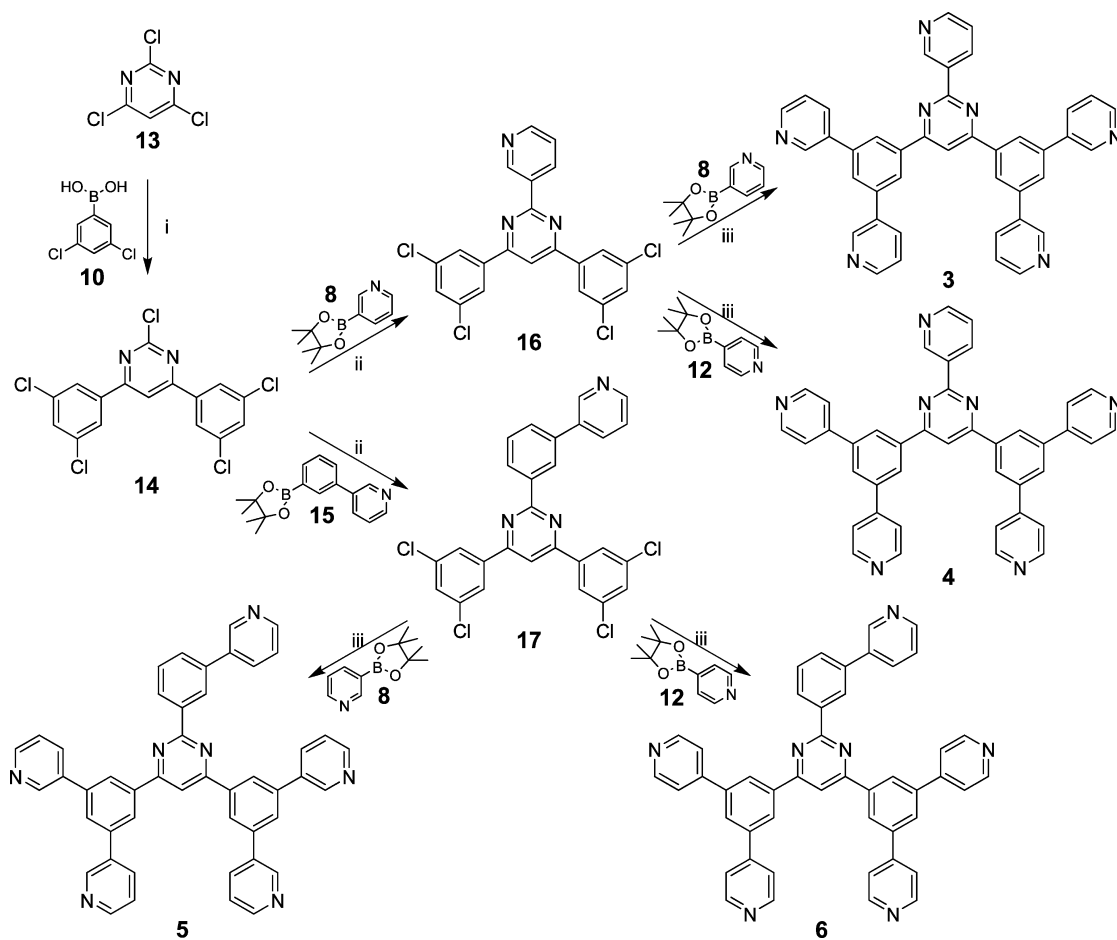
Density functional theory (DFT) calculations were also performed for the calculation of HOMO, LUMO, and triplet energy levels by using the Gaussian suite of programs (Gaussian 03W). The ground state ( $S_0$ ) structures were optimized with B3LYP/6-31G(d) method, and the single-point energies were calculated with B3LYP/6-311+G(d,p) method. In comparison, the lowest-energy triplet excited state ( $T_1$ ) structure optimization and single-point energy calculation were performed with UB3LYP/6-31G(d) and UB3LYP/6-311+G(d,p) methods, respectively.

**Device Fabrication and Characterization.** OLEDs were grown on a glass substrate precoated with a  $\sim 110$  nm thick layer of ITO having a sheet resistance of 15  $\Omega$ /square. The substrates were cleaned with ultrapurified water and organic solvents and then dry-cleaned for 20 min by exposure to an UV–ozone ambient. To improve the hole injection from the anode, poly(arylene amine ether sulfone)-containing tetraphenylbenzidine (TPDPES) doped with 10% (by weight) tris(4-bromophenyl) aminium hexachloroantimonate (TBPAH) was spun onto the precleaned substrate from its

Scheme 1. Synthetic Routes of Pyridine-Containing Compounds 1 and 2. i.  $\text{Pd}(\text{PPh}_3)_4$ , 2M  $\text{K}_2\text{CO}_3$ , or  $\text{Na}_2\text{CO}_3$ , Toluene/Ethanol; ii.  $\text{Pd}_2(\text{dba})_3$ ,  $\text{PCy}_3$ ,  $\text{K}_3\text{PO}_4$ , 1,4-Dioxane/Water



Scheme 2. Synthetic Routes of Pyridine- and Pyrimidine-Containing Compounds 3–6. i.  $\text{PdCl}_2(\text{PPh}_3)_2$ ,  $\text{K}_2\text{CO}_3$ , Acetonitrile/Water; ii.  $\text{PdCl}_2(\text{PPh}_3)_2$ ,  $\text{K}_2\text{CO}_3$ , Dioxane/Water; iii.  $\text{Pd}_2(\text{dba})_3$ ,  $\text{PCy}_3$ ,  $\text{K}_3\text{PO}_4$ , 1,4-Dioxane/Water



dichloroethane solution to form a 20-nm-thick polymer buffer layer.<sup>7</sup> Then, a 30-nm-thick HTL of 1,1-bis[4-[*N,N*-di(*p*-tolyl)-amino]phenyl]cyclohexane (TAPC) was deposited. Next, 8% (by weight)  $\text{Ir}(\text{PPy})_3$  was codeposited with *N,N'*-dicarbazolyl-4,4'-biphenyl (CBP) to form a 10-nm-thick EML. Finally, a 50-nm-thick ETL of 1–6 was

deposited to block holes and to confine excitons in the emissive zone. Cathodes consisting of a 0.5-nm-thick layer of LiF followed by a 100-nm-thick layer of Al were patterned using a shadow mask with an array of 2 mm × 2 mm openings. The electroluminescent (EL) spectra were taken by an optical multichannel analyzer, Hamamatsu PMA 11. The

current density and luminance versus driving voltage characteristics were measured by Keithley source-measure unit 2400 and Konica Minolta chroma meter CS-200, respectively. External quantum efficiencies were calculated from the luminance, current density, and EL spectrum, assuming a Lambertian distribution.

## RESULTS AND DISCUSSION

**Synthesis.** The developed ETMs are comprised of benzene, pyridine, and pyrimidine as building blocks, and they are combined with each other at their *meta*-positions to break their  $\pi$  conjugation. All the nitrogen atoms of pyridine rings are at the *meta*-position (refer to the combination sites) for **1**, **3**, and **5**. In contrast, one nitrogen atom is at the *meta*-position and the others are at the *para*-position for **2**, **4**, and **6**. Different from **1** and **2**, there is a pyrimidine ring in the center of **3–6**, and **5** and **6** are structurally different from **3** and **4** in one more phenyl inserted at the  $\alpha$ -position to two nitrogen atoms of the central pyrimidine, respectively.

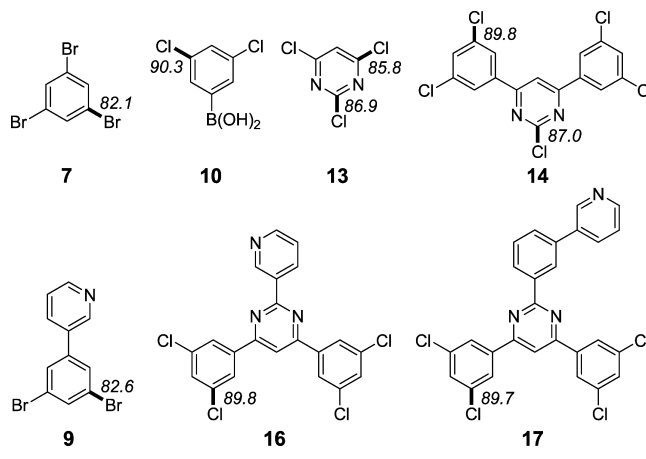
As shown in Scheme 1, the cross-coupling reaction of 1,3,5-tribromobenzene **7** with 1 equiv of 3-pyridine boronate ester **8** in the presence of catalytic amounts of Pd(PPh<sub>3</sub>)<sub>4</sub> and excess Na<sub>2</sub>CO<sub>3</sub> in a toluene/ethanol/water solvent system at 80 °C led to a 50% yield of 1,3-dibromo-5-pyrid-3-yl-benzene **9**, accompanied by a 16% yield of two-substituted byproduct of 1-bromo-3,5-dipyrid-3-yl-benzene **18**. Reaction of **9** with 3,5-dichlorophenyl boronic acid **10** led to a 66% yield of tetrachloride **11**. **11** was further coupled with an excess of **8**, in the presence of more effective catalyst system of Pd<sub>2</sub>(dba)<sub>3</sub> and PCy<sub>3</sub>, and excess K<sub>3</sub>PO<sub>4</sub> in a 1,4-dioxane/water solvent system to afford **1** in a yield of 82%.<sup>10</sup> Similarly, **2** was synthesized in a similar manner to that of **1** in a yield of 41% by coupling with 4-pyridine boronate ester **12**.

Different from **1** and **2**, there is a pyrimidine ring in the center of **3–6**, started from 2,4,6-trichloropyrimidine **13** (Scheme 2). Cross-coupling reaction of **13** with two equivalent of **10** in the presence of catalytic amounts of PdCl<sub>2</sub>(PPh<sub>3</sub>)<sub>2</sub> and excess K<sub>2</sub>CO<sub>3</sub> in an acetonitrile/water solvent system at 50 °C led to a 92% yield of 2-chloro-4,6-bis(3,5-dichlorophenyl)-pyrimidine **14**. Reaction of **14** with **8** in a 1,4-dioxane/water solvent system at an elevated temperature led to a 64% yield of tetrachloride **16**. Finally, **16** was coupled with an excess of pyridine boronate esters **8** and **12** in a similar manner to that of **1** and **2** to afford **3** in a yield of 87% and **4** in a yield of 82%, respectively. Similarly, reaction of **14** with pyrid-3-yl benzene boronate ester **15** led to a 67% yield of tetrachloride **17**. **17** was further coupled with an excess of **8** and **12** to afford **5** in a yield of 60% and **6** in a yield of 74%, respectively.

**Bond Dissociation Energy.** Selective sequential cross-coupling reactions involving multihalogenated aromatics is a particularly attractive approach to polysubstituted heterocycles that are of importance in pharmaceutical and manufacturing applications.<sup>11</sup> Knowles et al. reported that one source of selectivity is the nature of the halogen that is being displaced; iodine reacts before bromine, and bromine reacts before chlorine.<sup>12</sup> This originates from the significant differences in the carbon–halogen (C–X) bond strengths. Considering that the halogens being displaced are identical for the current reactants and intermediates, such as bromine for **4** and **6**, and chlorine for **8**, **11**, and **12**, there must be another factor that drives the regioselectivity in the current Suzuki cross-coupling reactions. Houk et al. reported that the regioselectivities in oxidation additions are controlled by the energy to distort a C–X bond to the transition state geometry, a factor related to the BDE.<sup>13</sup>

Although G3B3 was reported to be highly accurate and also has the fewest convergence problem, it is practically limited to only 10 heavy atoms (non-hydrogen atoms) and might not be applicable for most of the current reactants and intermediates.<sup>14</sup> Here, B3LYP was used to determine BDEs of the C–X bonds for the reactants and the intermediates.<sup>15</sup> Calculations demonstrate that **7** has a C–Br BDE of 82.1 kcal/mol, which is 0.5 kcal/mol lower than that of **9** coupled with a pyridine ring (Chart 1). It is predicted that **8** reacts primarily with **7** rather

**Chart 1.** Carbon–halogen (C–X) bond dissociation energies (BDEs) (kcal/mol) of reactants and intermediates calculated by B3LYP



than **9** to give a higher yield of **9** than **18**, which is consistent with the experimental result. In addition, **10** has a C–Cl BDE of 90.3 kcal/mol, which is much higher than the C–Br BDE of **9**, further indicating bromine reacts before chlorine to give a relatively high yield of the object intermediate **11**.

Calculations demonstrate that the 4- and 6-positions of **13** have lower C–Cl bond BDE of 85.8 kcal/mol than the 2-position (86.9 kcal/mol), and this is similar to that of 2,4-dichloropyrimidine,<sup>14</sup> indicating higher reactivity of C<sub>4</sub>–Cl and C<sub>6</sub>–Cl than C<sub>2</sub>–Cl. Considering C–Cl BDE of **10** is further higher than ones of **13**, **10** undergoes cross-coupling with **13** and reacts primarily with its 4- and 6-positions rather than its 2-position to give **14** in a high yield. For **14**, the C–Cl bond at the  $\alpha$ -position to two nitrogen atoms of pyrimidine has a BDE of 87.0 kcal/mol, which is quite similar to that of **13** at C<sub>2</sub> and is 2.8 kcal/mol lower than that at the benzene ring. As a result, cross-coupling reactions of **14** with functionalized boranes of **8** and **15** give the  $\alpha$ -position coupled products of **16** and **17** in relatively high yield with the same catalyst system but higher reaction temperature. Similar to **10** and **14**, C–Cl BDEs at the benzene ring of **16** and **17** are much higher than that at the pyrimidine, a more effective catalyst system such as Pd<sub>2</sub>(dba)<sub>3</sub>, PCy<sub>3</sub>, and K<sub>3</sub>PO<sub>4</sub> is necessary for their cross-coupling reactions with boronate esters. As a result, cross-coupling reactions of tetrachloride of **11**, **16**, and **17** with pyridine boronate esters give **1–6** in relatively high yield. Benefit from the sequential regioselective cross-coupling reactions, pyridine-containing compounds with different pyridine substitution positions in a single molecule, such as **2**, **4**, and **6**, were successfully synthesized for the first time. We have reported that the nitrogen atom position of the substituted pyridine ring is a key factor in determining the electron injection and transport property and thus the OLED performance.<sup>8</sup> The current

achievements would enable us to finely tune the property of the heterocycle-containing ETMs and to thoroughly understand their structure–property relationships.

**Physical Properties.** As an ideal ETM that can act as an ETL as well as a hole-block layer, it should possess a low-lying lowest unoccupied molecular orbital (LUMO) energy level to give a low electron injection barrier and a low-lying highest occupied molecular orbital (HOMO) energy level to block hole leakage from the EML. The calculated HOMO and LUMO energy levels of 1–6 are summarized in Table 1. For 1

**Table 1. Calculated HOMO and LUMO Energy Levels, HOMO–LUMO Band Gaps ( $E_g$ ), and Adiabatic Triplet Energies ( $T_1-S_0$ ) of 1–6 (B3LYP/6-311+G(d,p)//B3LYP/6-31G(d)) (All Values Reported in eV)**

compd	HOMO	LUMO	$E_g$	$T_1-S_0$
1	6.66	1.83	4.83	2.95
2	6.90	2.08	4.82	2.98
3	6.81	2.47	4.33	2.94
4	7.13	2.69	4.43	2.96
5	6.52	2.49	4.03	2.92
6	6.78	2.65	4.13	2.96

containing a *meta*-terphenyl core and five pyrid-3-yls combined at its *meta*-positions as the periphery, its LUMO energy level is lower-lying than that of a general electron-transport and hole-block material of 2,9-dimethyl-4,7-diphenylphenanthroline (BCP) (LUMO = 1.71 eV), and it also has deeper HOMO energy level than BCP (HOMO = 6.07 eV),<sup>16</sup> predicting improved electron-injection and hole-block property compared with BCP from the calculations. For 2 containing a pyrid-3-yl and four pyrid-4-yls, its HOMO and LUMO energy levels are 0.24 and 0.25 eV lower-lying than those of its analogue 1, respectively, by solely introducing four pyrid-4-yls instead of pyrid-3-yls. By introducing a pyrimidine ring instead of their central benzene, further lower-lying HOMO and LUMO energy levels are obtained for 3 and 4. LUMO energy levels of 5 and 6 are slightly influenced by introducing a phenyl at the  $\alpha$ -position to two nitrogen atoms of pyrimidine in comparison with 3 and 4, respectively, although their HOMO energy levels are  $\sim$ 0.3 eV higher-lying. Moreover, adiabatic triplet energies ( $T_1-S_0$ ) of 1–6 are estimated to be over 2.9 eV, which are ca. 0.3 eV higher than that of BCP,<sup>8b</sup> suggesting improved triplet energy confinement when used as an ETL as well as an exciton-block layer adjacent to the EML of the phosphorescent OLEDs.

UV–vis absorption spectrum of 1 exhibits a peak at 262 nm, which can be attributed to its  $\pi-\pi^*$  transition (Figure 1). Different from 1, there are absorption shoulders at 320 and 342 nm in combination with an absorption peak at 254 nm for 3, which can be attributed to the  $n-\pi^*$  transitions according to the central diphenylpyrimidine skeleton. The absorption shoulders due to the  $n-\pi^*$  transitions shift to the longer wavelengths of 326 and 346 nm for 5 due to one more phenyl inserted at the  $\alpha$ -position to two nitrogen atoms of pyrimidine that induces an elongated  $\pi$  conjugation. Narrower optical band gaps ( $E_g^{\text{opt}}$ ) were obtained in the order of 1 > 3 > 5 due to the bathochromic shift in UV–vis absorption spectrum (Table 2), which is consistent with the calculation results (Table 1). Similar phenomenon was also found for the compounds 2, 4, and 6 containing pyridine rings with different substituted positions, but the substituted positions of the pyridine rings

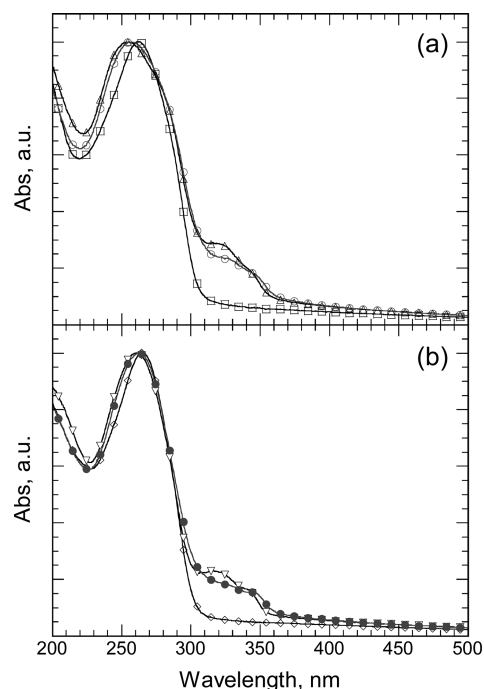


**Figure 1.** UV–vis absorption spectra of the vacuum-deposited films of 1 (□), 2 (◇), 3 (△), 4 (▽), 5 (○), and 6 (●) on quartz substrates.

**Table 2. Physical Properties of 1–6**

compd	$T_m^a$ (°C)	$T_g^a$ (°C)	$T_d^b$ (°C)	HOMO <sup>c</sup> (eV)	LUMO <sup>d</sup> (eV)	$E_g^{\text{opte}}$ (eV)
1	278	136	497	6.68	2.68	4.00
2	269	157	506	6.42	2.42	4.00
3	309	139	498	6.57	3.10	3.47
4	359	170	505	6.51	3.01	3.50
5	300	129	507	6.65	3.21	3.44
6	378	n.d.	517	6.62	3.17	3.45

<sup>a</sup>Glass transition temperature ( $T_g$ ) and melting temperature ( $T_m$ ) obtained from differential scanning calorimetry (DSC) measurement. <sup>b</sup>Decomposition temperature ( $T_d$ ) obtained from thermogravimetric analysis (TGA). <sup>c</sup>HOMO energy level approximated by atmospheric ultraviolet photoelectron spectroscopy (Rikken Keiki AC-3). <sup>d</sup>LUMO energy level approximated from HOMO energy level and optical band gap ( $E_g^{\text{opt}}$ ). <sup>e</sup>Optical band gap ( $E_g^{\text{opt}}$ ) estimated from the lowest energy absorption edge of the UV–vis absorption spectrum.

seem influence the absorption spectra and thus the energy band gaps vary slightly.

The experimental results indicate that the LUMO energy level of 1 is 2.68 eV, which is higher-lying than that of 3. Considering the only structural difference between 1 and 3 is the central pyrimidine ring. The lower-lying LUMO energy level achieved for 3 can be attributed to strong electron affinity of the central pyrimidine. The density functional theory (DFT)<sup>15</sup> calculations indicate that LUMO of 3 is mainly located at the central diphenyl pyrimidine skeleton and HOMO is mainly located at the outer dipyrindyl phenyl skeleton (Figure 2), proving that the lower-lying LUMO energy level of 3 is due to the strong electron affinity of the central pyrimidine. Similarly, a reduced LUMO energy level is achieved for 4 compared with 2. By introducing one more phenyl at the  $\alpha$ -position to two nitrogen atoms of pyrimidine, further reduced LUMO energy levels are achieved for 5 and 6, accompanied with slightly reduced HOMO energy levels. Although the

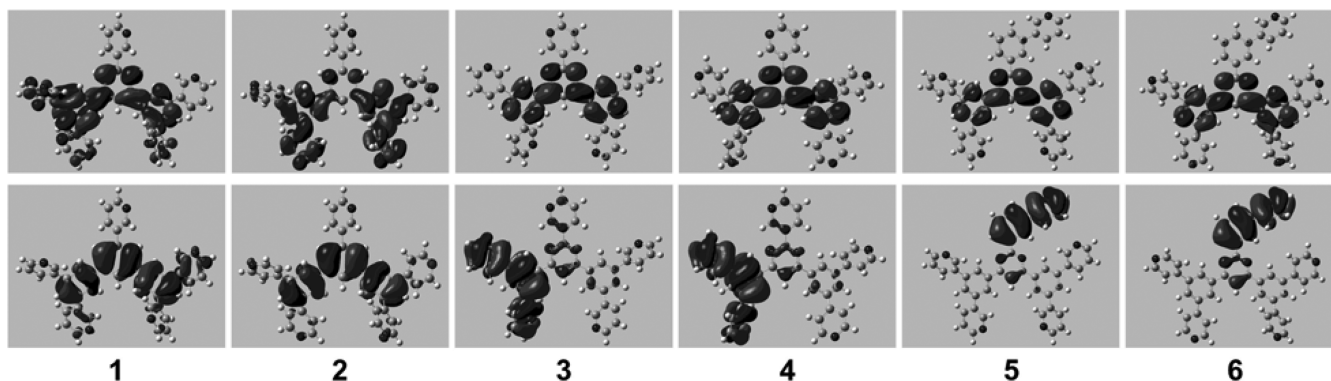


Figure 2. Calculated frontier orbitals of the HOMO (bottom) and LUMO (top) of 1–6.

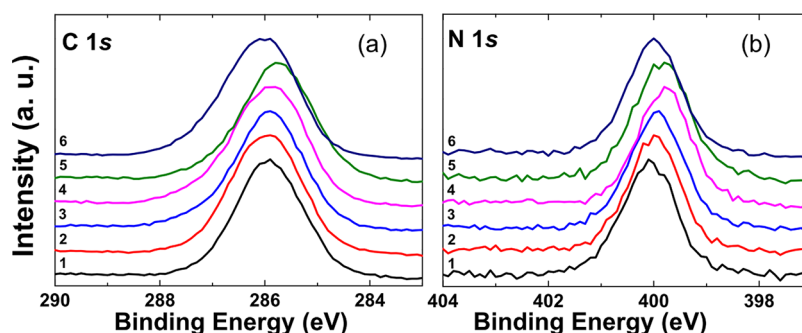


Figure 3. (a) C 1s and (b) N 1s regions of the XPS spectra for thin film samples of ETMs 1–6.

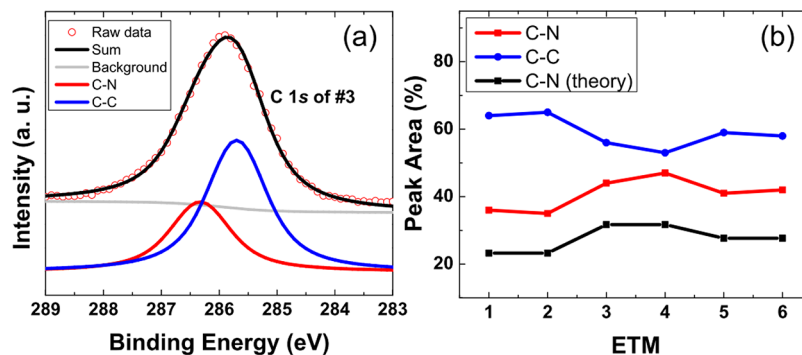


Figure 4. (a) Curve fitting for C 1s of thin film sample of ETM 3. (b) Peak area of the two C species (C–N and C–C) for thin film samples of ETMs 1–6.

introduction of one more phenyl for 5 and 6, similar to 3 and 4, their LUMOs are also mainly located at the central diphenyl pyrimidine skeleton. However, their HOMOs are mainly located at the pyridyl phenyl combined at the  $\alpha$ -position to two nitrogen atoms of pyrimidine.

Improved thermal properties were also achieved to give higher melting temperature ( $T_m$ ) and glass transition temperature ( $T_g$ ) by introducing pyrimidine as the core, and it can be attributed to the increased polarity and thus stronger molecular interaction. It was previously reported that no  $T_g$  was detected for the similar compounds containing pyridine due to the strong C–H $\cdots$ N hydrogen bonding interaction in the solid state.<sup>8b,16,17</sup> It is of interest that all the current compounds show  $T_g$  higher than 120 °C except for 6. It can be partly attributed to the introduction of pyrid-3-yl or pyrid-3-yl phenyl at the  $\alpha$ -position to two nitrogen atoms of pyrimidine to give a reduced molecular symmetry and thus a reduced intermolecular hydrogen bonding interaction. The high  $T_g$  values of the

current compounds prove the high morphologic stability of the amorphous phase in a deposited film, which is a prerequisite for their applications in OLEDs.

In Figure 3, parts a and b show C 1s and N 1s regions of the XPS spectra for thin film samples of ETMs 1–6. In Figure 3a, thin film samples of ETMs 1, 2, 3, and 4 show the binding energy of 285.9 eV at the maximum intensity. However, thin film samples of ETMs 5 and 6 show the binding energies of 285.7 and 286.0 eV, respectively. In Figure 3b, the binding energies of N 1s peaks at the maximum intensity are 400.1, 400.0, 399.9, 399.8, 399.8, and 400.0 eV, respectively.

To further understand the XPS data, we performed curve fitting for C 1s spectra using Doniach–Sünjić curves convoluted with Gaussian distribution of 0.6 eV full-width at half-maximum.<sup>18</sup> The background due to inelastic scattering was subtracted by the Shirley (or integral) method.<sup>19</sup> Figure 4a shows an example of curve fitting for the thin film sample of ETM 3. The red circles in Figure 4a represent the raw data.

The Shirley background (gray solid line in Figure 4a) was subtracted, followed by the curve fitting with two peaks corresponding to carbon species in 3, that is, C–N (red line) and C–C (blue line). Because the electronegativity of the N atom (3.04) is significantly stronger than that of the C atom (2.55), the peak corresponding to C–N is expected to have a higher binding energy than the peak corresponding to C–C. Lorentzian width and Gaussian width are fixed to be 0.90 and 0.64 eV, respectively, based on the Au 4f curve fitting for an independent Au thin film sample. The peak position and intensity of the two peaks are used as fitting parameters to obtain the final total signal (black line in Figure 4a). We performed similar curve fitting for all samples. Note that, for 3–6, there exists a third carbon species N–C–N. However, only one carbon atom (out of 41 carbon atoms per molecule) has this configuration, which is beyond the detection limit of the XPS system used in this study. Therefore, only two major carbon species are considered in the discussion hereafter. Figure 4b shows the integrated area under the two carbon peaks (in percent). As expected, the two curves change in opposite directions to maintain the sum of the two area values to be 100%. Black squares in Figure 4b represent the calculated C–N peak area. There is a striking similarity between the experimental curve and the theory curve, although they are offset by approximately 13% possibly due to strong intermolecular interactions in solid state films.

**Device Application.** It has been reported that the green phosphorescent OLEDs based on Ir(PPy)<sub>3</sub> exhibit the lowest driving voltage among the previously reported phosphorescent OLEDs. To study the electron injection and transport property of the developed materials, devices in an architecture of ITO/TPDPES (20 nm)/TAPC (30 nm)/CBP: 8 wt % Ir(PPy)<sub>3</sub> (10 nm)/1–6 (50 nm)/LiF (0.5 nm)/Al (100 nm) were fabricated by using 1–6 as a nondoped ETL as well as a hole/exciton-block layer; that is, there is no other hole/exciton-block layer inserted between the EML and the ETL, which is indispensable for the *p-i-n* OLEDs. In addition, a 0.5-nm-thick layer of LiF followed by a 100-nm-thick layer of Al is used as the cathode. The same as our previously reported green phosphorescent OLEDs, TPDPES is used as the hole-injection buffer layer, and TAPC is used as the HTL.<sup>7d</sup>

For the device based on 1, a threshold voltage ( $V_{th}$ ) of 2.5 V for current and a turn-on voltage ( $V_{on}$ ) of 2.7 V for electroluminescence (luminance of 1 cd m<sup>-2</sup> was detected) were obtained. In comparison with the device based on 1, although  $V_{th}$  and  $V_{on}$  for the device based on 2 are 0.1 V lower, driving voltages for higher luminance are much higher due to the higher-lying LUMO energy level of 2 and thus a high electron injection barrier. Driving voltages of the devices significantly decreased by utilizing 3 and 4 as an ETL (Figure 5). An ultralow  $V_{th}$  of 2.0 V and  $V_{on}$  of 2.2 V were achieved for the device based on 3, both are 0.5 V lower than those of the device based on 1. Considering the only structural difference between 1 and 3 is the central pyrimidine ring in 3, the reduced driving voltage can be attributed to the lower-lying LUMO energy level of 3 according to the pyrimidine ring with a strong electron affinity. By introducing four pyrid-4-yls instead of the pyrid-3-yls combined with the phenyls in 3 to give 4, further reduced  $V_{on}$  of 2.1 V was achieved for the device based on 4.

As formerly mentioned, the ideal operating voltage of OLEDs should approximately correspond to the photon energy ( $h\nu$ ) of the emitted photons. In fact, most of the ever reported classical OLEDs were far above in terms of operating voltage.

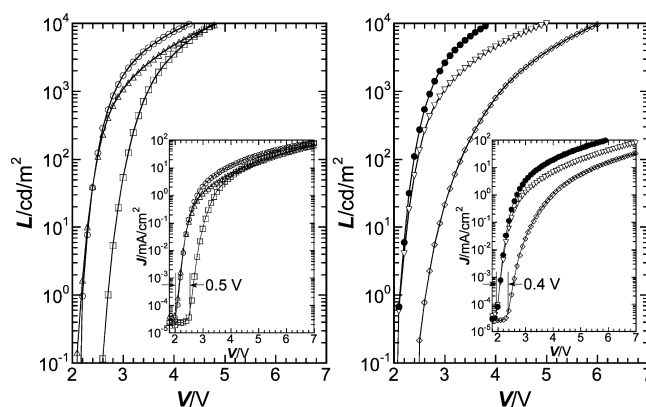


**Figure 5.** Luminance ( $L$ ) and current density ( $J$ ) (inset) versus operating voltage ( $V$ ) characteristics of the devices: ITO/TPDPES (20 nm)/TAPC (30 nm)/CBP: 8 wt % Ir(PPy)<sub>3</sub> (10 nm)/ETMs (50 nm)/LiF (0.5 nm)/Al (100 nm). ETMs: 1 (□), 2 (◇), 3 (△), 4 (▽), 5 (○), and 6 (●).

As shown in Figure 6, electroluminescent (EL) spectra of all the current devices are identical with a peak at 514 nm and a

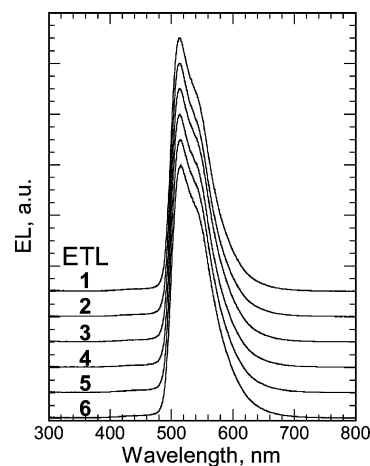


**Figure 6.** Electroluminescence (EL) spectra of the devices: ITO/TPDPES (20 nm)/TAPC (30 nm)/CBP: 8 wt % Ir(PPy)<sub>3</sub> (10 nm)/ETMs (50 nm)/LiF (0.5 nm)/Al (100 nm). ETMs: 1–6.

shoulder at 550 nm. Note that the emitted photon energy corresponding to the peak emission wavelength of 514 nm is 2.41 eV, and the average photon energy of the emitted light for the Ir(PPy)<sub>3</sub>-based device is  $\sim$ 2.3 eV. It is of interest that the threshold voltage  $V_{on}$  for electroluminescence of the current OLEDs is readily 0.2–0.3 V lower than the minimum value of  $h\nu/e$ , and a similar phenomenon has also been experimentally found for the inorganic light-emitting diodes.<sup>20</sup> By introducing a phenyl at the  $\alpha$ -position to two nitrogen atoms of pyrimidine to give 5, although the on-set voltages for current and electroluminescence are almost the same as those of the device based on 3, at a display-relevant luminance of 100 cd m<sup>-2</sup>, decreased driving voltage of 2.47 V was achieved for the device based on 5. In comparison, the lowest operating voltage for a typical luminance of 100 cd m<sup>-2</sup> for the Ir(PPy)<sub>3</sub>-based green phosphorescent *p-i-n* OLEDs is 2.65 V,<sup>6</sup> which is nearly 0.2 V higher than the current one. Even at an illumination-relevant luminance of 1000 cd m<sup>-2</sup>, the operating voltage is as low as 2.83 V. By introducing four pyrid-4-yls instead of four pyrid-3-yls of 5 to give 6, further reduced driving voltages of 2.39 and

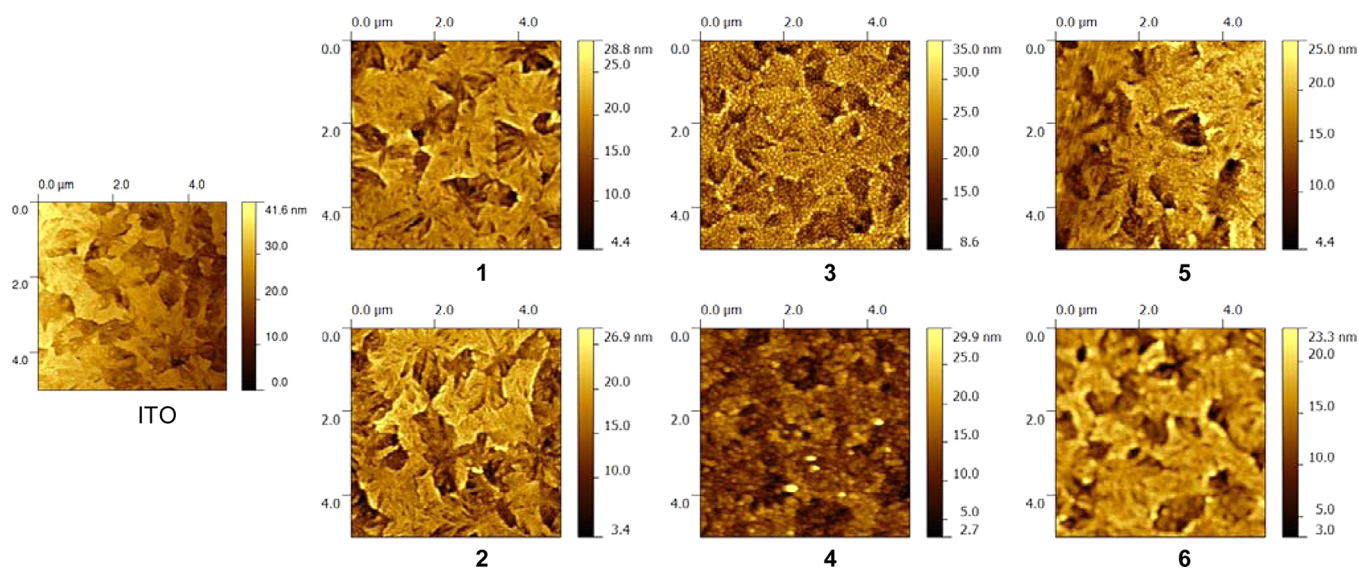


**Figure 7.** AFM images of the bare ITO substrate and the thin films of 1–6 vacuum deposited on ITO.

2.72 V were achieved for the device based on 6 at 100 and 1000  $\text{cd m}^{-2}$ , respectively, which are the lowest driving voltages for the green phosphorescent OLEDs hitherto,<sup>7d</sup> including the ever reported *p-i-n* OLEDs.<sup>6</sup> Although the current driving voltage for 100  $\text{cd m}^{-2}$  is already corresponding to the emitted photon energy, it is not the theoretical limit yet. As inspected by Leo et al., in an ideal device the quasi-Fermi-level spread is identical to the voltage applied to the contacts of the device, the theoretical voltage necessary to reach 1 and 100  $\text{cd m}^{-2}$  for green light is as low as 1.83 and 1.95 V, respectively.<sup>5</sup> In comparison, the turn-on voltage and the operating voltage for 100  $\text{cd m}^{-2}$  for the device based on 6 are only 0.27 and 0.44 V above the thermodynamic limits, respectively. Considering that the exciton binding energy might need some extra energy, the driving voltage achieved by 6 is very close to the thermodynamic limit, especially at low brightness. Moreover, even at a much brighter luminance of 10 000  $\text{cd m}^{-2}$ , a driving voltage as low as 3.88 V was also achieved.

It is well-known that, aside from the LUMO energy level and the electron injection barrier, the electron mobility may also play an important role in reduced operating voltage. Unfortunately, we failed in obtaining clear transient current by using general time-of-flight (TOF) technique and thus electron mobility of the current ETMs. Nevertheless, we have previously found that electron mobility as high as  $10^{-4} \sim 10^{-3} \text{ cm}^2 \text{ V}^{-1} \text{ s}^{-1}$  can be achieved for the pyridine-containing ETMs like triphenylbenzene derivatives.<sup>8a</sup> Figure 7 shows the AFM images of the bare ITO substrate after rigorous cleaning and the thin films of ETMs 1–6. It can be seen that the morphologies of the films of 1 and 2 are nearly conformal to the underlying ITO substrates. In contrast, for the films of 3–6 with a pyrimidine core fine structures can be identified, which may result from the well-ordered molecular domain structures in these samples. Such structures are expected to be favorable for electron hopping due to the strong intermolecular interaction such as  $\pi$ – $\pi$  stacking. Interestingly, lower driving voltages were achieved for the devices that are based on the ETMs containing a pyrimidine core.

Besides the unprecedented low operating voltage, an improved carrier balance was also achieved for the current devices based on the ETMs containing a pyrimidine ring. As

shown in Figure 8, improved current efficiency (CE) is achieved for the device based on 3 with a pyrimidine core in

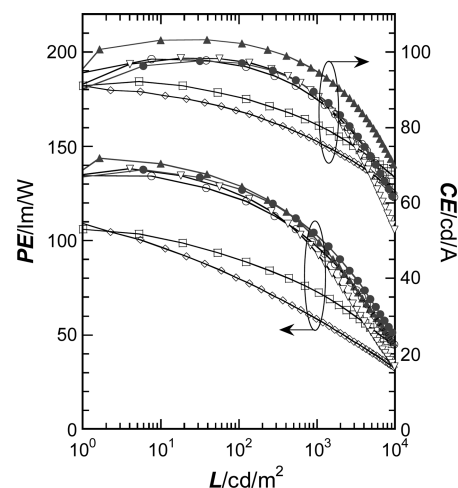


**Figure 8.** Power efficiency (PE) and current efficiency (CE) versus luminance ( $L$ ) characteristics of the devices: ITO/TPDPES (20 nm)/TAPC (30 nm)/CBP: 8 wt % Ir(PPy)<sub>3</sub> (10 nm)/ETMs (50 nm)/LiF (0.5 nm)/Al (100 nm). ETMs: 1 ( $\square$ ), 2 ( $\diamond$ ), 3 ( $\blacktriangle$ ), 4 ( $\nabla$ ), 5 ( $\circ$ ), and 6 ( $\bullet$ ).

comparison with 1 with a benzene core due to the improved carrier balance. Considering the reduced operating voltage and the improved current efficiency, aside from the improved electron injection and transport, the hole injection and transport must also be improved when 3 is used as the ETL. The improved electron injection may induce an aggregation of electron at the cathode side and thus an increased internal electric field. The hole injection and transport from the anode should be accelerated due to the increased electric field despite the same HTL and buffer layer utilized. Although CE of the device based on 5 slightly decreased compared with the device based on 3, it is still higher than the device based on 1 at the luminance lower than 5000  $\text{cd m}^{-2}$ . A similar phenomenon was also found for the devices based on the ETMs of 2, 4, and 6 containing pyridine rings with different substitution positions. Among these ETMs, the highest CE of 102 and 94.9  $\text{cd A}^{-1}$ ,

**Table 3. Summary of Performance Data of the Devices: ITO/TPDPES (20 nm)/TAPC (30 nm)/CBP: 8 wt % Ir(PPy)<sub>3</sub> (10 nm)/ETMs (50 nm)/LiF (0.5 nm)/Al (100 nm). ETMs: 1–6**

ETMs	$V_{\text{on}}$ (V)	at 100 cd m <sup>-2</sup>				at 1000 cd m <sup>-2</sup>			
		V (V)	PE (lm W <sup>-1</sup> )	CE <sub>e</sub> (cd A <sup>-1</sup> )	$\eta_{\text{ext}}$ (%)	V (V)	PE (lm W <sup>-1</sup> )	CE (cd A <sup>-1</sup> )	$\eta_{\text{ext}}$ (%)
1	2.7	3.07	90.3	88.1	24.6	3.48	72.8	80.7	22.5
2	2.6	3.32	79.8	84.3	23.5	4.11	58.3	76.2	21.3
3	2.2	2.49	129	102	28.5	2.97	100	94.9	26.4
4	2.1	2.45	125	97.6	27.2	2.98	93.3	88.4	24.6
5	2.2	2.47	123	96.5	26.8	2.83	97.1	87.5	24.3
6	2.1	2.39	128	97.0	26.9	2.72	103	89.0	24.6

corresponding to  $\eta_{\text{ext}}$  of 28.5% and 26.4%, were achieved at 100 and 1000 cd m<sup>-2</sup>, respectively, for the 3-based device. Accompanied with the low operating voltage, high power efficiency (PE) of 129 and 100 lm W<sup>-1</sup> were achieved at 100 and 1 000 cd m<sup>-2</sup>, respectively. In comparison, the devices based on 4–6 exhibit relatively lower CE of  $\sim 97$  and  $\sim 88$  cd A<sup>-1</sup> at 100 and 1 000 cd m<sup>-2</sup>, respectively. Although CE of the device based on 6 is somewhat lower than that of the device based on 3, a comparable PE of 128 lm W<sup>-1</sup> was achieved at 100 cd m<sup>-2</sup> due to the reduced driving voltage. In addition, at an illumination-relevant luminance of 1000 cd m<sup>-2</sup>, a higher PE of 103 lm W<sup>-1</sup> was achieved (Table 3). Compared with the previously reported green phosphorescent OLEDs in the same architecture that exhibit very low operating voltage,<sup>7d</sup> the device based on 6 exhibits further lower operating voltage and higher  $\eta_{\text{ext}}$  further proving simultaneous reduced operating voltage and improved carrier balance can be achieved by the development of an ETM with improved electron injection and transport. Note that no light-out coupling technology was used in this work, and all the efficiencies were recorded from the forward view. This means that there is still a big room for further improvement of electroluminescent efficiency and decrement of operating voltage of the current devices by various light-out coupling technologies.<sup>21</sup> Considering that the  $\eta_{\text{ext}}$  of the device with the lowest driving voltage is still somewhat lower than the device based on 3, there is also some other room for further improvement of power efficiency by the improvement of  $\eta_{\text{ext}}$  to the high limit without any voltage drops, and further optimization of hybrid heterocycle-containing ETMs should be an effective route to realize it.

## CONCLUSIONS

In summary, a series of hybrid heterocycle-containing ETMs with different pyridine substitution positions in a single molecule were developed by regioselective sequential palladium-catalyzed Suzuki cross-coupling reactions. The two carbon species associated with C–N and C–C can be detected by X-ray photoelectron spectroscopy. B3LYP calculations exhibit the experimental regioselectivity is conceivably consistent with the quantitative trends in BDEs of the C–X bonds of aryl halides. Similar to the inorganic light-emitting diodes, extremely low turn-on voltage for electroluminescence, which is 0.2–0.3 V lower than the minimum value of  $h\nu/e$ , was experimentally achieved by utilizing the developed ETMs as an electron-transport and hole/exciton-block layer for the classical Ir(PPy)<sub>3</sub>-based green phosphorescent OLEDs. Moreover, hitherto the lowest operating voltage of 2.39 V for 100 cd m<sup>-2</sup> that is already corresponding to the emitted photon energy ( $h\nu$ ) was achieved with simultaneously improved external quantum efficiency to give high power efficiency by utilizing 6 as an ETL. Atomic force microscopy measurements reveal

morphological fine structure of the thin film samples of ETMs with a pyrimidine core, which possibly contributes to the low driving voltages that were achieved for the devices that are based on these ETMs. These findings indicate that aside from the ultralow operating voltage well-balanced carriers can be also achieved with a finely synthesized ETM as a nondoped ETL, and the B3LYP calculation is an effective method to predict the regioselective cross-coupling reactions for fine design of such an ETM.

## AUTHOR INFORMATION

### Corresponding Author

\*E-mail: mssjsu@scut.edu.cn (S.J.S.), yabing.qi@oist.jp (Y.B.Q.).

### Notes

The authors declare no competing financial interest.

## ACKNOWLEDGMENTS

S.J.S. greatly appreciates the financial support from the National Natural Science Foundation of China (51073057), the Ministry of Science and Technology (2009CB930604 and 2011AA03A110), the Ministry of Education (NCET-11-0159), and the Fundamental Research Funds for the Central Universities (2011ZZ0002). Y.B.Q. and M.C.J. acknowledge the support from an internal grant of Okinawa Institute of Science and Technology Graduate University. The authors acknowledge Chemipro Kasei Kaisha Limited for TPDPES.

## REFERENCES

- (1) (a) Kido, J.; Iizumi, Y. *Appl. Phys. Lett.* **1998**, *73*, 2721. (b) Okumoto, K.; Kanno, H.; Hamaa, Y.; Takahashi, H.; Shibata, K. *Appl. Phys. Lett.* **2006**, *89*, 063504.
- (2) (a) Baldo, M. A.; O'Brien, D. F.; You, Y.; Shoustikov, A.; Sibley, S.; Thompson, M. E.; Forrest, S. R. *Nature (London)* **1998**, *395*, 151. (b) Baldo, M. A.; Lamansky, S.; Burrows, P. E.; Thompson, M. E.; Forrest, S. R. *Appl. Phys. Lett.* **1999**, *75*, 4. (c) Wong, W.-Y.; Ho, C.-L. *Coord. Chem. Rev.* **2009**, *253*, 1709. (d) Wong, W.-Y.; Ho, C.-L. *J. Mater. Chem.* **2009**, *19*, 4457.
- (3) (a) Kido, J.; Matsumoto, T. *Appl. Phys. Lett.* **1998**, *73*, 2866. (b) Watanabe, S.; Agata, Y.; Tanaka, D.; Kido, J. *J. Photopolym. Sci. Technol.* **2005**, *18*, 83.
- (4) (a) Huang, J.; Pfeiffer, M.; Werner, A.; Blochwitz, J.; Leo, K. *Appl. Phys. Lett.* **2002**, *80*, 139. (b) Pfeiffer, M.; Forrest, S. R.; Leo, K.; Thompson, M. E. *Adv. Mater.* **2002**, *14*, 1633. (c) Matsushima, T.; Adachi, C. *Appl. Phys. Lett.* **2006**, *89*, 253506. (d) Meerheim, R.; Walzer, K.; Pfeiffer, M.; Leo, K. *Appl. Phys. Lett.* **2006**, *89*, 061111.
- (5) Meerheim, R.; Walzer, K.; He, G.; Pfeiffer, M.; Leo, K. *Proc. SPIE* **2006**, *6192*, 61920P.
- (6) He, G.; Pfeiffer, M.; Leo, K.; Hofmann, M.; Birnstock, J.; Pudziel, R.; Salbeck, J. *Appl. Phys. Lett.* **2004**, *85*, 3911.
- (7) (a) Su, S.-J.; Chiba, T.; Takeda, T.; Kido, J. *Adv. Mater.* **2008**, *20*, 2125. (b) Su, S.-J.; Tanaka, D.; Li, Y.-J.; Sasabe, H.; Takeda, T.; Kido,

J. *Org. Lett.* **2008**, *10*, 941. (c) Xiao, L.; Su, S.-J.; Agata, Y.; Lan, H.; Kido, J. *Adv. Mater.* **2009**, *21*, 1271. (d) Su, S.-J.; Sasabe, H.; Pu, Y.-J.; Nakayama, K.; Kido, J. *Adv. Mater.* **2010**, *22*, 3311.

(8) (a) Su, S.-J.; Takahashi, Y.; Chiba, T.; Takeda, T.; Kido, J. *Adv. Funct. Mater.* **2009**, *19*, 1260. (b) Sasabe, H.; Tanaka, D.; Yokoyama, D.; Chiba, T.; Pu, Y.-J.; Nakayama, K.; Yokoyama, M.; Kido, J. *Adv. Funct. Mater.* **2011**, *21*, 336.

(9) Moulder, J. F.; Stickle, W. F.; Sobol, P. E.; Bomben, K. D. *Handbook of X-ray Photoelectron Spectroscopy*; Physical Electronics: Eden Prairie, MN, 1995.

(10) Kudo, N.; Perseghini, M.; Fu, G. C. *Angew. Chem., Int. Ed.* **2006**, *45*, 1282.

(11) (a) Schröter, S.; Stock, C.; Bach, T. *Tetrahedron* **2005**, *61*, 2245.

(b) Fairlamb, I. J. S. *Chem. Soc. Rev.* **2007**, *36*, 1036.

(12) Knowles, J. P.; Whiting, A. *Org. Biomol. Chem.* **2007**, *5*, 31.

(13) Legault, C. Y.; Garcia, Y.; Merlic, C. A.; Houk, K. N. *J. Am. Chem. Soc.* **2007**, *129*, 12664.

(14) Garcia, Y.; Schoenebeck, F.; Legault, C. Y.; Merlic, C. A.; Houk, K. N. *J. Am. Chem. Soc.* **2009**, *131*, 6632.

(15) Frisch, M. J.; Trucks, G. W.; Schlegel, H. B.; Scuseria, G. E.; Robb, M. A.; Cheeseman, J. R.; Montgomery, Jr., J. A.; Vreven, T.; Kudin, K. N.; Burant, J. C.; Millam, J. M.; Iyengar, S. S.; Tomasi, J.; Barone, V.; Mennucci, B.; Cossi, M.; Scalmani, G.; Rega, N.; Petersson, G. A.; Nakatsuji, H.; Hada, M.; Ehara, M.; Toyota, K.; Fukuda, R.; Hasegawa, J.; Ishida, M.; Nakajima, T.; Honda, Y.; Kitao, O.; Nakai, H.; Klene, M.; Li, X.; Knox, J. E.; Hratchian, H. P.; Cross, J. B.; Bakken, V.; Adamo, C.; Jaramillo, J.; Gomperts, R.; Stratmann, R. E.; Yazyev, O.; Austin, A. J.; Cammi, R.; Pomelli, C.; Ochterski, J. W.; Ayala, P. Y.; Morokuma, K.; Voth, G. A.; Salvador, P.; Dannenberg, J. J.; Zakrzewski, V. G.; Dapprich, S.; Daniels, A. D.; Strain, M. C.; Farkas, O.; Malick, D. K.; Rabuck, A. D.; Raghavachari, K.; Foresman, J. B.; Ortiz, J. V.; Cui, Q.; Baboul, A. G.; Clifford, S.; Cioslowski, J.; Stefanov, B. B.; Liu, G.; Liashenko, A.; Piskorz, P.; Komaromi, I.; Martin, R. L.; Fox, D. J.; Keith, T.; Al-Laham, M. A.; Peng, C. Y.; Nanayakkara, A.; Challacombe, M.; Gill, P. M. W.; Johnson, B.; Chen, W.; Wong, M. W.; Gonzalez, C.; Pople, J. A. *Gaussian 03, Revision D.01*; Gaussian, Inc.: Wallingford, CT, 2004.

(16) Sasabe, H.; Chiba, T.; Su, S.-J.; Pu, Y.-J.; Nakayama, K.; Kido, J. *Chem. Commun.* **2008**, 5821.

(17) Tanaka, D.; Sasabe, H.; Li, Y.-J.; Su, S.-J.; Takeda, T.; Kido, J. *Jpn. J. Appl. Phys., Part 2* **2007**, *46*, L10.

(18) Doniach, S.; Sünjić, M. *J. Phys. C* **1970**, *3*, 285.

(19) Shirley, D. A. *Phys. Rev. B* **1972**, *5*, 4709.

(20) Schubert, E. F. *Light-Emitting Diodes*, 2nd ed.; Cambridge University Press: Cambridge, 2006; pp 83–85.

(21) (a) Sun, Y.; Forrest, S. R. *Nat. Photonics* **2008**, *2*, 483.

(b) Reineke, S.; Lindner, F.; Schwartz, G.; Seidler, N.; Walzer, K.; Lüssem, B.; Leo, K. *Nature (London)* **2009**, *459*, 234. (c) Helander, M. G.; Wang, Z. B.; Qiu, J.; Greiner, M. T.; Puzzo, D. P.; Liu, Z. W.; Lu, Z. H. *Science* **2011**, *332*, 944.